Tidal influence on flow dynamics of Dotson Ice Shelf, West Antarctica

Gabriela Collao-Barrios[1,2], Ted A. Scambos[3], Christian T. Wild[4,5], Martin Truffer[6], Karen E. Alley[7], and Erin C. Pettit[4]

[1]National Snow and Ice Data Center, CIRES, University of Colorado Boulder
[2]IGE, Universite Grenoble Alpes
[3]Earth Science and Observation Center, CIRES, University of Colorado Boulder
[4]College of Earth, Ocean, and Atmospheric Sciences, Oregon State University, Corvallis OR, USA
[5]Department for Geoscience, University of Tübingen, Tübingen, Germany
[6]University of Alaska Fairbanks
[7]University of Manitoba

Correspondence: Gabriela Collao-Barrios (gabriela.collao-Barrios@univ-grenoble-alpes.fr)

Abstract. On Dotson Ice Shelf, Antarctica, ice velocities derived from satellite image pairs and in-situ GPS measurements reveal an oscillating flow pattern that is correlated with tide height. The tidally-affected flow pattern is of limited extent, in an area near the Wunneberger Rock nunatak in the outflow of Kohler Glacier. Comparing variations in the region's flow velocity derived from a series of 16-day repeat-pass Landsat 8 image pairs spanning 2014-2020, and a 64-hour GPS record in 2022 with the CATS2008 and TPXO9 tide-height models, indicates a significant correlation between tidal uplift and the direction of ice-flow. During high-tide periods the ice-shelf flows in a true north direction, while at low-tide periods flow direction shifts towards the northeast, marking an approximately 40° change in flow direction. GPS measurements describe a continuous corkscrew-like motion of the ice-shelf surface, confirming the link between tide height and ice-flow direction. We attribute the observed pattern to tidally controlled changes of buttressing along the ice-shelf margins and the fin-like shape of Wunneberger Rock. This leads to a dual pattern: (i) fast flow across the grounding line of the tributary Kohler Glacier during high tides aligning with Wunneberger Rock's summit ridge; and (ii) slow flow during low tide height facing its flanks. We suggest that the link between tides and ice dynamics is related to the rapid ice-shelf thinning in the area. In light of the continued thinning of ice shelves surrounding Antarctica, we anticipate similar variations in flow direction and speed arising from changes in tidal influence on buttressing from pinning points and grounding zones.

1 Introduction

Ice shelves are key components of glacier outlet systems, providing a resisting stress on glacier flow through interaction with ice rises, ice rumples and their lateral shear margins (Thomas, 2004; Dupont and Alley, 2005; Matsuoka et al., 2015; Still et al., 2019). Therefore, ice shelves play a crucial role in governing ice-sheet discharge. Destabilization of ice shelves, or their entire collapse, frequently leads to significant glacier acceleration and greater ice-mass discharge, thereby affecting rates of sea-level rise (Scambos et al., 2004; Rignot et al., 2005; Dupont and Alley, 2005; Scambos et al., 2014; Johannes J. Fürst, 2016).

Dotson Ice Shelf is located on the western side of Antarctica's Amundsen Sea Embayment (Fig. 1). Known for having one of the highest rates of ice thinning due to basal melt and grounding-line retreat around Antarctica, the Dotson Ice Shelf, along with its neighboring Crosson Ice Shelf and their tributary glaciers, has been a focus of research (Lilien et al., 2018; Milillo et al., 2022; Wild et al., 2022b). Originally mapped as two separate ice shelves in the 1960s with 'Bear Peninsula' acting as a divide (USGS map reference 1968), it was later discovered, at least as early as the 1990s, that Bear 'Peninsula' was indeed an island. . This revelation united the Dotson and Crosson ice shelves into a single contiguous floating ice plate (Rignot et al., 2011; Scheuchl et al., 2016), Fig.1. The Dotson-Crosson system is influenced by numerous ice rises and rumples, including a fin-like nunatak protruding through the central Dotson Ice Shelf named Wunneberger Rock (Lilien et al., 2018).

High basal melt rates observed beneath Dotson Ice Shelf arise from the presence of modified Circumpolar Deep Water (mCDW) near the glacier grounding lines (Shepherd et al., 2004; Pritchard et al., 2012). Recent changes in the flux of mCDW into the near-coastal regions of the Amundsen Sea are thought to stem from changes in regional wind patterns and their impact on isopycnal depth at the continental shelf break (Steig et al., 2012; Holland et al., 2019; Dotto et al., 2020; Holland et al., 2020).

The rapid basal melt has driven dramatic changes in the Dotson-Crosson ice-shelf system over recent decades. For example, as the ice-shelf has undergone thinning, the grounding lines of Pope and Smith Glaciers have retreated by tens of kilometers, as observed by InSAR mapping spanning 1992 through 2020 (Milillo et al., 2022). The grounding line of Kohler Glacier retreated between 1996 and 2011, followed by re-advancement until 2014 (Scheuchl et al., 2016; Khazendar et al., 2016; Lilien et al., 2018). Within the former 'Bear Peninsula' boundary, which historically delineated the Dotson-Crosson system into two separate ice shelves, the areal extent of several ice rumples has shrunk and several of them have disappeared since the 1990s (Scheuchl et al., 2016), Fig.1. These changes have led to significant glacier acceleration and reorganization of flow (Wild et al., 2022b). Ice-flow speeds in the Crosson section of the ice-shelf system remain high, up to 1 km a^{-1}. In the Dotson sector, ice-flow speed is generally below 400 m a^{-1}, with the exception of the Kohler Glacier grounding zone, where ice flows around 500 m a^{-1} in the main trunk. Two important pinning points, Wunneberger Rock (WR; see Fig. 1) and an ice rumple referred to as D6 (Scheuchl et al., 2016), upstream of WR, limit nearby ice-flow to between 200-300 m a^{-1}. Along the flow paths from Smith East and Smith West glacier outlets, the ice significantly accelerated between 1996 and 2014 (Lilien et al., 2018) and then decelerated thereafter. Kohler Glacier experienced a similar acceleration (1994-2000) followed by deceleration since 2009 (Wild et al., 2022b).

In addition to driving high basal melt and changes in ice dynamics, the ocean influences the Dotson-Crosson system through tides. Ocean tides can modulate flow speeds of ice streams and glaciers through several mechanisms: changes in basal shear stress underneath the grounded ice (Gudmundsson, 2006), subglacial pressure variations (Walker et al., 2013), changing ice-shelf buttressing (Rosier and Gudmundsson, 2018), changes in pinning point buttressing (Robel et al., 2017), and periodic (un)grounding of some parts of the ice-shelf (Minchew et al., 2017). Unexpected tidal responses can emerge in grounded systems with low basal shear stress (Winberry et al., 2014). In a few cases, high tides can lift floating ice completely off lightly grounded ice rumples, temporarily eliminating the basal resistance to flow (Brunt et al., 2011; Scheuchl et al., 2016; Robel

55 et al., 2017). Despite being inadequately constrained by in-situ observations, these mechanisms provide a crucial test case for understanding the large-scale drivers of ice discharge into the ocean (Padman et al., 2018).

This study presents insights into the influence of tides on the ice-flow dynamics of Dotson Ice Shelf and its interaction with the WR nunatak (Fig. 1). To investigate the relation between tidal heights and ice velocity changes we examine both regional multi-year velocity fields from satellites and local short-term measurements from in-situ GPS data. To identify the
60 mechanisms behind the correlation between tides and ice-flow changes, we analyze the surface and basal geometry surrounding Wunneberger Rock using airborne radar data. We calculate regional strain-rate variability and determine the effective resistance imposed by Wunneberger Rock. We then discuss the potential implications for further thinning of Dotson Ice Shelf.

2 Data and Methods

2.1 Multiyear spatially distributed satellite-based ice velocity data

65 We analyzed ice-shelf flow speed and direction using repeat ice-flow mappings from the GoLIVE dataset (Fahnestock et al., 2015; Scambos and Klinger., 2016) to identify changes in ice dynamics at a 16-day to multiyear scale (Figs. 3 and 4). GoLIVE ice velocity maps are generated through feature correlation tracking in Landsat 8 image pairs, with images separated by 16 to 400 days. Ice-flow vectors are determined on a 300 x 300 m grid with an estimated ice motion error equal to ± 0.1 m d^{-1} for image pairs separated by 16 days (assuming displacement errors of 0.1 pixels of the 15 m ground-equivalent size
70 of Landsat 8 panchromatic band pixels) sourced from https://www.nsidc.org. For assessing longer-term flow speed trends of Dotson Ice Shelf, we used the ITS_LIVE web tool, also accessible through nsidc.org (see also Gardner et al., 2018). Ice-flow speeds showed no trend in the downstream area of Dotson Ice Shelf over the Landsat 8-9 record in ITS_LIVE (November 2013 - January 2020, 377 ± 36 m a^{-1}, at 74.35°S, 112.5°W, 155 image pairs), nor any significant difference between the Landsat 8-9 velocity mappings and earlier point velocity assessments from the Coastal Change Map series (Swithinbank et al.,
75 2003). In our flow analysis of Dotson Ice Shelf, we focus on the Kohler Glacier inflow region, where we observed significant changes in the ice-flow direction pattern. This analysis used 23 pairs of 16-day-span velocity data from GoLIVE during the seven-year period 2014-2020, resolving more than 75% of the area. We classify the dataset into times when the 16-day period covers predominantly high or low tidal heights. The 25% quartile (q25) represents faster flow speed of the ice-shelf (and it is associated with high tide, as shown later) and the 75% quartile (q75) to represent slow flow (and low tide period). The quartiles
80 are based on ice-flow direction and we used the same quantiles for direction and speed.

2.2 Tidal cycle from models and comparison with Landsat image pair intervals

We modeled tidal heights for Dotson Ice Shelf with the CATS2008 Circum-Antarctic Inverse Tidal Model (Howat et al., 2019), an updated version of the model by (Padman et al., 2002) and TPXO9 model (Egbert and Erofeeva, 2002). Additionally, we derived an estimate of tidal loading on the Earth's crust from TPXO9 and the Inverse Barometric Effect (IBE) from ERA-5
85 pressure data (Hersbach et al., 2020).

2.3 Local short-term ice-flow variability from GPS

To further investigate the dynamic interaction between ice-flow velocity, Wunneberger Rock, and tides, as well as to validate tidal heights from models, we installed a GPS (GNSS receiver, NetR9 Trimble) on Dotson Ice Shelf. The station was located 8 km from Wunneberger Rock (74.74°S, 113.47°W; Fig. 2b), outside of its narrow tidal flexure zone, and operated continuously

90 over a 64-hour period from 8th to 11th January, 2022 as part of the International-Thwaites-Glacier-Collaboaration's TARSAN 2021-2022 field campaign (see www.thwaitesglacier.org). Dual-frequency phase data measurements from the receiver were recorded at 1 Hz and processed using the Canadian Spatial Reference System Precise Point Positioning (CSRS-PPP) service (https://webapp.csrs-scrs.nrcan-rncan.gc.ca/geod/tools-outils/ppp.php). The positions were converted from WGS84 latitude and longitude to Antarctic Polar Stereographic easting and northing (epsg:3031) using the pyproj library. Obvious outliers

95 (deviating more than 3 m from the vertical mean) were removed from the dataset. The resulting precision, based on the standard deviation of the high-pass filtered positions, is better than 0.01 m in both the horizontal and vertical directions. Subsequently, the data were rotated into a coordinate system with x pointing along the mean flow direction and y in the transverse direction. Finally, we smoothed the rotated coordinates with a temporal low-pass filter with a cutoff frequency of 5 minutes.

2.4 Radar Profiles

100 We use Multichannel Coherent Radar Depth Sounder (MCoRDS) profiles from IceBridge acquired in October 2018 (Paden et al., 2010, updated 2021) to depict the surface and subsurface geometry of Wunneberger Rock and the surrounding ice. The IRMCR1B 20181031_01_032 profile correspond to P1 in Fig.2c and profiles a and b in Fig. 9, and the IRMCR1B 20181031_01_033 profile corresponds to P2 in Fig. 2c and profiles c and d in Fig.9.

2.5 Strain rate estimation

105 We estimate strain rates using the logarithmic strain-rate code developed by Alley et al (2018). This method computes shear, longitudinal and transverse strain rates relative to the flow direction. The method is applied at the 300 m spatial resolution from GoLive ice velocities and thickness from BedMachine Antarctica Version 2 (Morlighem, 2020). To capture strain rates at small scales near rumples, Wunneberger Rock, and lateral ice-shelf margins, we employ length scale roughly equal to the ice thickness. The propagated strain rate errors in the Alley et al. (2018) logarithmic strain rate products are shown to be very

110 small (<1%) in shear margins, such as the area around Wunneberger Rock. Considering that the absolute error in the individual velocity pairs used in this study are typically an order of magnitude higher than the velocities in the stacked products used by Alley et al. (2018), we expect the propagated strain-rate error to also be an order of magnitude higher (<10%).

2.6 Effective resistance calculation

To study the impact of Wunneberger Rock on ice-shelf flow in terms of ice-flow direction and speed, we assess its effective

115 resistance using the methodology outlined by Still et al. (2019). The equation development can be found in Macayeal et al. (1987). The methodology separates the force (F) acting on a parcel of ice into two components: (i) the form drag (Ff), which

represents the depth integrated glaciostatic pressure in the absence of motion, and (ii) the dynamic drag (Fd), corresponding to the viscous stresses associated with motion. The objective is to estimate the contribution of glaciostatic stresses to backpressure.

We use this distinction to analyze separately the resistance stemming from Wunneberger Rock and from the different ice-flow directions and speeds. We estimate effective resistance following the formulation of Still et al. (2019), integrating the form drag, Ff from Eq.(1) to obtain Eq.(3), and dynamic drag, Fd in Eq.(3), by integrating stresses along the circumference of an elliptical vertical cylinder surrounding the Wunneberger Rock.

$$\overrightarrow{F_f} = \oint_\Gamma \left\{ \int_{zb}^{zs} \int_z^{zs} \rho(z) \, g \, dsdz \right\} \hat{n} d\lambda \tag{1}$$

Then, using the exponential density depth relation from Cuffey and Paterson 2010 (Eq.(2))

$$\rho(z) = \rho_i - \alpha \, exp(\beta(z_s - z)) \tag{2}$$

They obtained the following equation.

$$\overrightarrow{F_f} = \oint_\Gamma \left\{ \frac{1}{2}\rho_i gH^2 + \frac{\alpha}{\beta}gH + \frac{\alpha}{\beta^2}(1 - exp(\beta H)g) \right\} \hat{n} d\lambda \tag{3}$$

where ρ_i is the ice density = 910 kg m^{-3}, and the last two terms account for the firn density using the exponential density depth relation from Cuffey and Paterson 2010, Eq.(8). These and values are adjusted to match a density profile derived from seismic velocity measured in the upper Dotson area (Muto et al., in prep), = 600 kg m^{-3} and =-0.0364 m^{-1} assuming a regionally constant density profile. We use the ice thickness (H) from BedMachine Version 2 from Morlighem (2020). Our form drag estimates are sensitive to spatially variable density profiles and uncertainties in H, however they are a good approximation given the available data.

$$\overrightarrow{F_d} = \oint_\Gamma 2\overline{\nu^z}H \left\{ \dot{\epsilon_{ij}} \bullet \hat{n} + (\dot{\epsilon_{xx}} + \dot{\epsilon_{yy}})\hat{n} \right\} d\lambda \tag{4}$$

We use B=1.8*108 (Pa s^{-1})1/n from Wild et al. (2022a), which was estimated with an inverse method for the neighboring Thwaites Eastern Ice Shelf.

3 Results

3.1 Ice-flow velocity changes from spatially distributed data

Our multiyear analysis of ice-flow shows discernible changes in ice-flow direction and speed across a large area of Dotson Ice Shelf. Figure 3 presents the mean, along with the 25% and 75% quartiles of flow directions and speed derived from 23 pairs

of 16-day-span velocity data from GoLIVE, covering the seven-year period 2014-2020. The measured mean direction over the Kohler Glacier outflow area (depicted by the red delimited area in Figure 3a), shows flow direction changes of about 40° between the 25% and 75% quartiles in the area where the flow from Kohler Glacier merges with the central ice-shelf. This highlights two different behavioral patterns. . Speed also varies between the quartiles, with higher speeds observed in the 25%
145 quartile (q25) compared to the 75% quartile (q75). The largest variation, of about 0.3 m d-1 higher, occurs around and south of Wunneberger Rock, coinciding with the region of the largest directional changes and the grounding zone of Kohler Glacier. There is also some change in velocity flow from the small southeast tributary, however, it is mainly upstream of the grounding line (Fig. 3 e and f).

Looking closer at the affected area (Fig. 4), we can observe that the velocity vector is closely aligned with the orientation of
150 the Wunneberger Rock summit ridge when the flow is near 270° (Fig. 4b, q25). Conversely, when the flow is around 315° the ice is flowing in a partially transverse direction to the ridge and other ice rumple areas of Wunneberger Rock (Fig. 4c, q75).

To investigate whether changes in ice-flow are related to ocean tides, we look for correlations between flow direction, speed and the tidal cycle. However, we have to take into account that we are analyzing ice-flow direction and speed in a time span of 16 days. To correlate these variables effectively, we average the tidal height from the tide models over the 16-day time span
155 between Landsat images. An example of the method is shown in Figure 5. with a 4-month subset of the seven-year data. The horizontal magenta lines represent flow directions for each 16-day image pair, while average tidal heights for the corresponding time periods are shown as horizontal blue lines. The black line is the tidal height from CATS2008.

This analysis over the entire set revealed no significant correlation between ice speed and tide heights, with correlation coefficients R of -0.07 (pv=0.78) and -0.05 (pv=0.84), using CATS2008 and TPOX9 respectively. However, we identified a
160 low but statistically significant inverse correlation between the average ice-flow direction over the Kohler Glacier outflow area and time-averaged tidal heights, including IBE and tidal load. Using the TPOX9 model, the correlation coefficient was -0.43 (pv=0.04), while the CATS2008 model showed an R of -0.42 with a pv=0.048. Figure 5 shows that most of the flow directions are inversely correlated with time-averaged tidal heights, exemplified by pairs 1,2,3,4 and 5. However, pairs 6 and 7 show a more complex relation. In addition, note that these correlations are based on time-averaged values (16-day averages), which
165 attenuate the tidal signal and the more subtle motions revealed by the continuous GPS record, discussed next.

3.2 Analysis of GPS point ice-flow near Wunneberger Rock

We gain more insight into the relation between the flow direction changes and tides by analyzing the relationship between the horizontal direction of displacement and the height measured with the 64 hours of GPS data acquired from the ice-shelf surface. These measurements were taken during a period when the tidal amplitude was rising after a neap tide, with a pronounced
170 semi-diurnal component that only becomes noticeable at neap tides (Fig. 6). Despite this atypical measurement period, the observed horizontal flow direction and tide height demonstrate an anti-correlation (R=-0.36, pv <0.01), corroborating the low but significant relationship identified in the 16-day multi-year satellite data. However, the measured ice displacement is complex as can be seen in Figure 7. This visualization presents the 3D motion captured by the GPS, with colors indicating the height during the primary/dominant diurnal component. As in Figure 8, where the displacement is separated into vertical

175 motion, horizontal motion, and speed. Here, we focus our analysis on the diurnal component due to its predominant occurrence over time.

During the main diurnal component (depicted in colored periods in Figure 8a), horizontal flow directions follow a pattern consistent with the 16-day analysis, with a bearing of 270° at high tidal height (green colors) and a bearing ranging from around 315° at low tidal height (pink colors, Fig. 8b). However, during the semidiurnal periods, the ice displacement is even more

180 complex, occasionally opposing the mean flow direction (see Figure 7 during grey-line periods). Speed shows no correlation with tidal height, which is consistent with previous findings suggesting a nonlinear relationship between speed and tides (Robel et al., 2017). Analysis of the measured horizontal speed reveals ice-flow acceleration during three peaks coinciding with rising tides, except for the last one (black arrows, Fig. 8c). A three-dimensional video of the GPS motion is provided in Supplemental Movie SX.

185 Validation of the modeled tidal height using GPS data provided a root-mean-square-errors (RMSE) of 0.08 m and 0.09 m for CATS2008 and TPXO9, respectively. Those errors are negligible in comparison to the tidal amplitudes, with maximum values reaching about 1.5 m and an average amplitude of around 0.5 m, indicating that either tide model accurately captures the tidal oscillation. However, the GPS measurement duration is insufficient to validate the IBE. Nevertheless, the RMSE of TPOX9 + IBE is 0.17 m, consistent with the RMSE value obtained for the nearby Thwaites Eastern Ice Shelf (Wild et al., 2022a),

190 representing the nearest available data.

3.3 Ice and rock geometry

Wunneberger Rock nunatak has a shark-fin shape that protrudes through the ice-shelf surface in a NE-SW orientation, aligning closely with the mean flow direction. Its summit ridgeline is roughly aligned with bearing 270° (see Figures 3 and 4). Satellite imagery reveals several distinct crevassed regions, each with a unique morphology (Figure 2c). Towards the upstream end,

195 there are transverse-extensional rifts associated with re-grounding of the ice shelf, flow-divergence, and uplift of the ice plate against the ice rise, termed "inflow crevasses". Trailing the shark-fin outcrop, rifts indicative of extensional flow, referred to as 'scar crevasses', are observed. A smaller area of chaotic crevasses northeast of Wunneberger Rock appears to represent a second sub-parallel grounded ice rumple area, labelled as "ice rumple crevasses". For a comprehensive understanding of the rock shape below the ice-shelf surface, we analyze airborne radar profiles from Operation IceBridge (Paden et al. (2010,

200 updated 2021); https://nsidc.org).

The radar profiles confirm the remarkably steep flanks of the Wunneberger Rock nunatak (Fig. 9). Using the IceBridge data and our own interpretation of the internal stratigraphy we determined rock face angles of about 57° and 23° in profile a, and 41° and 23° in profile b. Due to the narrow configuration along its elongated axis and the particularly steep southeast face, the nunatak's impact on the ice-shelf is anticipated to vary significantly based on the direction of ice-flow. It tends to impede flow

205 in the transverse direction (that is, across the long axis of the shark-fin, when flow is more to the west) but has a much smaller effect on flow in the longitudinal direction (more easterly flow). The radar profiles show thicker ice on the southeast side of the rock ridge, where the ice-flow is generally incoming toward the ridge. In contrast, the ice thickness is noticeably thinner to the north and west of the nunatak.

3.4 Strain rate analysis

We distinguish two configurations of longitudinal and shear strain around Wunneberger Rock corresponding to the flow conditions of the 25% and the 75% quartiles (Fig. 10). For the q25 representing a flow direction of 270° and fast flow speed, correlated with high tidal height (Fig. 3b and e); therefore the longitudinal, shear and transverse strain rate at the pinning point are larger due to the higher speed (Fig. 10 a-c). For the q75, representing flow direction around 315° and slower flow, correlated with low tide (Fig. 10 d-f); the strain rates are smaller around the pinning point. Another difference between the two flow patterns is the change of sign on longitudinal strain rate at the northern border of the Kohler Glacier area (Fig. 10 a and d). These results underscore the impact of tidal height changes on the stresses exerted on the ice surrounding the rock.

Strain rates along the ice-shelf sides and within the grounding zone exhibit no discernible change between the two quartiles. To gain (further) insight into the observed dynamics, we investigated both a along-flow profile along the flow and a across-flow transect across the grounding zone (Fig 11). The longitudinal profile shows a flow acceleration from upstream to the grounding line, followed by a deceleration upon entering the floating ice. These findings are consistent in both quartiles, but the q25 shows higher flow speeds. This aligns with the extensional zone upstream of the grounding line and the downstream compression, evident in the longitudinal strain-rate transect.

The compression at the entrance into the floating ice highlights the ice-shelf's buttressing role on the tributary glacier. Following the deceleration, the speed is similar for both quartiles from 42 km to 48 km. Subsequently, the q75 pattern decelerates while q25 pattern maintains constant speed. The difference in speed beyond thirty kilometers downstream of the grounding line shows that the two ice-flow patterns arise both from differences in the grounding zone and buttressing effects along the lateral shear margins and pinning points of the ice shelf.

The across-flow profile in the grounding zone shows a similar longitudinal strain rate shape for both quartiles, 0.74 a^{-1} and 0.68 a^{-1} for q75 and q25, respectively. Since the acceleration and peak velocity are higher for q25, we assume that the basal shear stress is affected by tidal height and is higher for the lower tidal height configuration represented by q75, with lower velocities.

At the small south-east tributary a along-flow profile shows a speed flow change between the two quartiles only upstream of the grounding zone and when entering the common trunk at about 10 km after, with very small longitudinal stresses changes between the grounding zone and the common trunk (Fig. A1, in appendix), indicating no-significant influence on the regional flow.

3.5 Wunneberger Rock effective resistance

To study the impact of the Wunneberger Rock nunatak on the ice-shelf dynamics from the two different ice-flow patterns we estimated the resistive force of the rock for both the q25 and q75 quartiles (representing high and low tide behavior). The form drag is the same for both flow patterns, because it does not depend on the motion, it is only shape-dependent. Since the averaged tide height changed by only a few centimeters, we assume that the amount of rock surface in contact with the ice did not change significantly, yielding a consistent form drag. From Figure 12a we can observe that the components of the form

drag are larger at two sides of the ellipse, corresponding to two zones of ice thickening. The direction of the summed form drag is opposite to the flow direction from the 75% quartile shown by the higher impact on the rock restricting the flow from that direction, Figure 10b.

Figure 12c shows the dynamical drag elements from the q25 pointing mainly in a uniform direction while dynamical drag elements from the q75, in Figure 12e, show a more variable direction, due to a more complex velocity pattern. The summed dynamical drag is one order of magnitude larger for the q25 (1.15×10^{12} N) mainly because there is a larger shear strain than for the dynamical drag of the q75 (0.19×10^{12} N). They point in opposite directions, showing the contrasting resistance imposed by the rock from the different flow patterns. Because of the q25 dynamical drag vector direction, Figure 12d and g, the total drag is smaller than the total drag from the q75.

4 Discussion

4.1 Ice-flow changes

Our analysis indicates the existence of two alternating flow patterns in the Kohler glacier zone of Dotson Ice Shelf, with changes in the basal shear of the grounding zone, in the buttressing at ice-margin shear and pinning points on this zone. In particular, resistive force imposed by Wunneberger Rock at the center of the Kohler Glacier ice outflow changes with tidal height, leading to the observed change of flow direction.

We find a significant correlation between the flow direction changes and the tidal cycle, (R=0.42 or 0.43 for CATS2008 and TPOX9 models, respectively) that implies a dependence of flow direction on tidal stage of 18-19%. This is corroborated by the correlation we obtain with the GPS field measurement (R=0.36), which implies a dependency of 13% during the short period (and small tide amplitude) the GPS was collecting data.

The Wunneberger Rock effective resistance result shows that the drag vector direction is opposite to the 75% quartile of flow directions (q75, low tide periods), related to low tide height velocity pattern showing that the rock resistance mainly acts in that direction. Also, the total drag magnitude is higher for the 75% quartile of flow vectors, representing a larger resistance when the ice-flow shows this behavior.

When we look to speed, the image-pair velocity tracking indicates faster flow for the q25 (related to high tide heights) than for the q75 (related to low tides). This is particularly true at the grounding zone, indicating probably a reduction of basal shear stress at high tide.

Details of the GPS motion show a complex but highly repetitive relationship between tide height and flow speed, particularly in the last two tidal cycles in our record (Fig. 8). Subtle, brief increases and decreases in flow speed are matched in the tide cycle, periods of faster flow are mainly at rising tide height with the exception of the last high speed peak. This implies a far more detailed and complex interaction with the feature, but a full explanation would require a dataset over a much longer period of time. We also note that much greater amplitude of tide interaction occurs in a full tidal cycle that was not captured during the GPS data collection period.

As shown in Figure 13, the Wunneberger Rock feature comprises the shark-fin nunatak (highlighted in yellow in Figure 13) and two ice rumple areas, one just in front of the fin feature to the southwest, and one downstream of the fin to the northeast. Radar profiles of the shark-fin feature (Fig. 6) show that it is very steep, and satellite images show that it is nearly aligned with the fast flow (q25 pattern), and related to high tide height. During high tide periods, faster flow coming from the grounding zone of Kohler Glacier aligns with the shark-fin-like nunatak and ice rumples areas. The resistance to flow across the feature overall is reduced because the flow orientation is more aligned (as we estimated with the resistive force analysis) and probably also due a weaker contact with the ice rumple areas, related to a higher ice bottom elevation. During low tide, ice-flow is slower and flow direction around the pinning point is less consistent, with more resistance from the Wunneberger rock and, especially evident in the GPS data, a far more complex ice motion behavior.

4.1.1 Tide impact and ice-shelf thinning

Our satellite-derived ice velocity record is not long enough (not at the precision required) to analyze when the tide-related flow variations began. Other satellites data sources (that extend earlier than 2013, with Landsat 8's launch) do not have the necessary temporal resolution (16-days) to be able to capture this short-term flow change. However, we infer that, due to the rapid pace of ice-shelf thinning (e.g., Khazendar et al. (2016)), and the frequent changes in contact with ice rumples, tides are having a large impact on the buttressing in ice-shelf borders and pinning points on the Dotson Ice Shelf. In particular, on the Kohler Glacier outflow area, the "Kohler Rumple" (Fig. 1) lost contact with the ice-shelf in 2011 (it disappeared from visible-band imagery). We suspect that after that time, the Wunneberger Rock nunatak interaction with the ice-shelf dynamics changed and the two alternate patterns that we find today began.

5 Conclusions

Our results show a relation between tides and flow direction that result from changes in the ice margins and around a nunatak/ice rumple region, Wunneberger Rock. There is also grounding-zone acceleration from tidally-driven changes in stresses at the ice margins and the nunatak. Estimated shear-strain rates and resistive forces confirm these changes in ice-rock contact stress induced by tides.

We hypothesize that as a result of rapid thinning of the Dotson Ice Shelf and the disappearance of the D6 pinning point, tidal effects on the resistive forces around Wunneberger Rock became more significant, and the periodic changes in ice-flow began.

Here we found new evidence of how tides can influence ice-shelf dynamics, not only in speed but also in horizontal direction. This link between tides and ice dynamics around ice rumples or ice rises may occur in more areas with further, widespread ice-shelf thinning.

Data availability. The satellite ice velocity data use in this study is freely available at https://www.nsidc.org. The computed strain-rate maps and the GPS record will be accessible through the USAP-DC upon acceptance of this article (https://www.usap-dc.org/view/project/p0010162).

Video supplement. A video showing the GPS displacement will available upon acceptance of this article:
305 (https://www.usap-dc.org/view/project/p0010162).

Author contributions. GCB analyzed the data, wrote the manuscript and participated in fieldwork. TS contributed to the initial idea and was the scientific leader on the field work. CW conducted tide modeling and participated on the field work. MT did the GPS data analysis. And all the authors contributed with the analysis and writing.

Competing interests. All authors declare that this study has no competing interests or conflicts of interest to disclose.

310 *Acknowledgements.* This study was supported by a Landsat Science Team award for cryosphere research (USGS contract 140G0118C0005) and the NSFPLR-NERC award for the ITGC TARSAN project (NSF-NERC 1738992). We thanks NSF, USAP, Nicolas Bayou from Earthscope and Kenn Borek Air for the field work support.

References

Alley, K. E., Scambos, T. A., Anderson, R. S., Rajaram, H., Pope, A., and Haran, T. M.: Continent-wide estimates of Antarctic strain rates from Landsat 8-derived velocity grids, Journal of Glaciology, 64, 321–332, https://doi.org/10.1017/jog.2018.23, 2018.

Brunt, K. M., Fricker, H. A., and Padman, L.: Analysis of ice plains of the Filchner–Ronne Ice Shelf, Antarctica, using ICESat laser altimetry, Journal of Glaciology, 57, 965–975, https://doi.org/10.3189/002214311798043753, 2011.

Dotto, T. S., Naveira Garabato, A. C., Wåhlin, A. K., Bacon, S., Holland, P. R., Kimura, S., Tsamados, M., Herraiz-Borreguero, L., Kalén, O., and Jenkins, A.: Control of the Oceanic Heat Content of the Getz-Dotson Trough, Antarctica, by the Amundsen Sea Low, Journal of Geophysical Research: Oceans, 125, e2020JC016113, https://doi.org/https://doi.org/10.1029/2020JC016113, e2020JC016113 2020JC016113, 2020.

Dupont, T. K. and Alley, R. B.: Assessment of the importance of ice-shelf buttressing to ice-sheet flow, Geophysical Research Letters, 32, https://doi.org/https://doi.org/10.1029/2004GL022024, 2005.

Egbert, G. D. and Erofeeva, S. Y.: Efficient Inverse Modeling of Barotropic Ocean Tides, Journal of Atmospheric and Oceanic Technology, 19, 183 – 204, https://doi.org/10.1175/1520-0426(2002)019<0183:EIMOBO>2.0.CO;2, 2002.

Fahnestock, M., Scambos, T., Moon, T., Gardner, A., Haran, T., and Klinger, M.: Rapid large-area mapping of ice flow using Landsat 8, Remote Sensing of Environment, https://doi.org/10.1016/j.rse.2015.11.023, 2015.

Förste, C., Bruinsma, S., Abrikosov, O., Flechtner, F., Marty, J.-C., Lemoine, J.-M., Dahle, C., Neumayer, H., Barthelmes, F., König, R., and Biancale, R.: EIGEN-6C4 - The latest combined global gravity field model including GOCE data up to degree and order 1949 of GFZ Potsdam and GRGS Toulouse, in: EGU General Assembly Conference Abstracts, EGU General Assembly Conference Abstracts, p. 3707, 2014.

Gardner, A. S., Moholdt, G., Scambos, T., Fahnstock, M., Ligtenberg, S., van den Broeke, M., and Nilsson, J.: Increased West Antarctic and unchanged East Antarctic ice discharge over the last 7 years, The Cryosphere, 12, 521–547, https://doi.org/10.5194/tc-12-521-2018, 2018.

Gudmundsson, G. H.: Fortnightly variations in the flow velocity of Rutford Ice Stream, West Antarctica, Nature, 444, 1063–1064, https://api.semanticscholar.org/CorpusID:4362662, 2006.

Hersbach, H., Bell, B., Berrisford, P., Hirahara, S., Horányi, A., Muñoz-Sabater, J., Nicolas, J., Peubey, C., Radu, R., Schepers, D., Simmons, A., Soci, C., Abdalla, S., Abellan, X., Balsamo, G., Bechtold, P., Biavati, G., Bidlot, J., Bonavita, M., De Chiara, G., Dahlgren, P., Dee, D., Diamantakis, M., Dragani, R., Flemming, J., Forbes, R., Fuentes, M., Geer, A., Haimberger, L., Healy, S., Hogan, R. J., Hólm, E., Janisková, M., Keeley, S., Laloyaux, P., Lopez, P., Lupu, C., Radnoti, G., de Rosnay, P., Rozum, I., Vamborg, F., Villaume, S., and Thépaut, J.-N.: The ERA5 global reanalysis, Quarterly Journal of the Royal Meteorological Society, 146, 1999–2049, https://doi.org/https://doi.org/10.1002/qj.3803, 2020.

Holland, D. M., Nicholls, K. W., and Basinski, A.: The Southern Ocean and its interaction with the Antarctic Ice Sheet, Science, 367, 1326–1330, https://doi.org/10.1126/science.aaz5491, 2020.

Holland, P. R., Bracegirdle, T. J., Dutrieux, P., Jenkins, A., and Steig, E. J.: West Antarctic ice loss influenced by internal climate variability and anthropogenic forcing, Nature Geoscience, 12, 718–724, https://doi.org/10.1038/s41561-019-0420-9, 2019.

Howat, I. M., Porter, C., Smith, B. E., Noh, M.-J., and Morin, P.: The Reference Elevation Model of Antarctica, The Cryosphere, 13, 665–674, https://doi.org/10.5194/tc-13-665-2019, 2019.

Johannes J. Fürst, Gaël Durand, F. G.-C. L. T. R. M. B. M. G. O.: The safety band of Antarctic ice shelves, Nature Climate Change, https://doi.org/10.1038/nclimate2912, 2016.

350 Khazendar, A., Rignot, E., Schroeder, D. M., Seroussi, H., Schodlok, M. P., Scheuchl, B., Mouginot, J., Sutterley, T. C., and Velicogna, I.: Rapid submarine ice melting in the grounding zones of ice shelves in West Antarctica, Nature Communications, 7, 13 243, https://doi.org/10.1038/ncomms13243, 2016.

Lilien, D. A., Joughin, I., Smith, B., and Shean, D. E.: Changes in flow of Crosson and Dotson ice shelves, West Antarctica, in response to elevated melt, The Cryosphere, 12, 1415–1431, https://doi.org/10.5194/tc-12-1415-2018, 2018.

355 Macayeal, D., Bindschadler, R., Shabtaie, S., Stephenson, S., and Bentley, C.: Force, Mass, and Energy Budgets of the Crary Ice Rise Complex, Antarctica, Journal of Glaciology, 33, 218–230, https://doi.org/10.3189/S0022143000008728, 1987.

Matsuoka, K., Hindmarsh, R. C., Moholdt, G., Bentley, M. J., Pritchard, H. D., Brown, J., Conway, H., Drews, R., Durand, G., Goldberg, D., Hattermann, T., Kingslake, J., Lenaerts, J. T., Martín, C., Mulvaney, R., Nicholls, K. W., Pattyn, F., Ross, N., Scambos, T., and Whitehouse, P. L.: Antarctic ice rises and rumples: Their properties and significance for ice-sheet dynamics and evolution, Earth-Science Reviews, 150,
360   724–745, https://doi.org/https://doi.org/10.1016/j.earscirev.2015.09.004, 2015.

Milillo, P., Rignot, E., Rizzoli, P., Scheuchl, B., Mouginot, J., Bueso-Bello, J. L., Prats-Iraola, P., and Dini, L.: Rapid glacier retreat rates observed in West Antarctica, Nature Geoscience, 15, 48–53, https://doi.org/10.1038/s41561-021-00877-z, 2022.

Morlighem, M.: MEaSUREs BedMachine Antarctica, Version 2, https://doi.org/10.5067/E1QL9HFQ7A8M, 2020.

Paden, J., Li, J., Leuschen, C., Rodriguez-Morales, F., and Hale., R.: IceBridge MCoRDS L2 Ice Thickness, Version 1,
365   https://doi.org/10.5067/GDQ0CUCVTE2Q, 2010, updated 2021.

Padman, L., Fricker, H. A., Coleman, R., Howard, S., and Erofeeva, L.: A new tide model for the Antarctic ice shelves and seas, Annals of Glaciology, 34, 247–254, https://doi.org/10.3189/172756402781817752, 2002.

Padman, L., Siegfried, M. R., and Fricker, H. A.: Ocean Tide Influences on the Antarctic and Greenland Ice Sheets, Reviews of Geophysics, 56, 142–184, https://doi.org/https://doi.org/10.1002/2016RG000546, 2018.

370 Pritchard, H. D., Ligtenberg, S. R. M., Fricker, H. A., Vaughan, D. G., van den Broeke, M. R., and Padman, L.: Antarctic ice-sheet loss driven by basal melting of ice shelves, Nature, 484, 502–505, https://doi.org/10.1038/nature10968, 2012.

Rignot, E., Casassa, G., Gogineni, S., Kanagaratnam, P., Krabill, W., Pritchard, H., Rivera, A., Thomas, R., Turner, J., and Vaughan, D.: Recent ice loss from the Fleming and other glaciers, Wordie Bay, West Antarctic Peninsula, Geophysical Research Letters, 32, https://doi.org/https://doi.org/10.1029/2004GL021947, 2005.

375 Rignot, E., Mouginot, J., and Scheuchl, B.: Antarctic grounding line mapping from differential satellite radar interferometry, Geophysical Research Letters, 38, https://doi.org/https://doi.org/10.1029/2011GL047109, 2011.

Rignot, E., Mouginot, J., Morlighem, M., Seroussi, H., and Scheuchl, B.: Widespread, rapid grounding line retreat of Pine Island, Thwaites, Smith, and Kohler glaciers, West Antarctica, from 1992 to 2011, Geophysical Research Letters, 41, 3502–3509, https://doi.org/https://doi.org/10.1002/2014GL060140, 2014.

380 Robel, A. A., Tsai, V. C., Minchew, B., and Simons, M.: Tidal modulation of ice shelf buttressing stresses, Annals of Glaciology, 58, 12–20, https://doi.org/10.1017/aog.2017.22, 2017.

Rosier, S. H. R. and Gudmundsson, G. H.: Tidal bending of ice shelves as a mechanism for large-scale temporal variations in ice flow, The Cryosphere, 12, 1699–1713, https://doi.org/10.5194/tc-12-1699-2018, 2018.

Scambos, T., M. F. T. M. A. G. and Klinger., M.: Global Land Ice Velocity Extraction from Landsat 8 (GoLIVE), Version 1,
385   https://doi.org/10.7265/N5ZP442B, 2016.

Scambos, T. A., Bohlander, J. A., Shuman, C. A., and Skvarca, P.: Glacier acceleration and thinning after ice shelf collapse in the Larsen B embayment, Antarctica, Geophysical Research Letters, 31, https://doi.org/https://doi.org/10.1029/2004GL020670, 2004.

Scambos, T. A., Berthier, E., Haran, T., Shuman, C. A., Cook, A. J., Ligtenberg, S. R. M., and Bohlander, J.: Detailed ice loss pattern in the northern Antarctic Peninsula: widespread decline driven by ice front retreats, The Cryosphere, 8, 2135–2145, https://doi.org/10.5194/tc-8-2135-2014, 2014.

Scheuchl, B., Mouginot, J., Rignot, E., Morlighem, M., and Khazendar, A.: Grounding line retreat of Pope, Smith, and Kohler Glaciers, West Antarctica, measured with Sentinel-1a radar interferometry data, Geophysical Research Letters, 43, 8572–8579, https://doi.org/https://doi.org/10.1002/2016GL069287, 2016.

Shepherd, A., Wingham, D., and Rignot, E.: Warm ocean is eroding West Antarctic Ice Sheet, Geophysical Research Letters, 31, https://doi.org/https://doi.org/10.1029/2004GL021106, 2004.

Steig, E., Ding, Q., Battisti, D., and Jenkins, A.: Tropical forcing of Circumpolar Deep Water Inflow and outlet glacier thinning in the Amundsen Sea Embayment, West Antarctica, Annals of Glaciology, 53, 19–28, https://doi.org/10.3189/2012AoG60A110, 2012.

Still, H., Campbell, A., and Hulbe, C.: Mechanical analysis of pinning points in the Ross Ice Shelf, Antarctica, Annals of Glaciology, 60, 32–41, https://doi.org/10.1017/aog.2018.31, 2019.

Swithinbank, C., Williams Jr., R. S., Ferrigno, J. G., Foley, K. M., and Rosanova, C. E.: Coastal-change and glaciological map of the Bakutis Coast, Antarctica: 1972-2002, Tech. rep., Reston, VA, https://doi.org/10.3133/i2600F, report, 2003.

Thomas, R. H.: Force-perturbation analysis of recent thinning and acceleration of Jakobshavn Isbræ, Greenland, Journal of Glaciology, 50, 57–66, https://doi.org/10.3189/172756504781830321, 2004.

Walker, R. T., Parizek, B. R., Alley, R. B., Anandakrishnan, S., Riverman, K. L., and Christianson, K.: Ice-shelf tidal flexure and subglacial pressure variations, Earth and Planetary Science Letters, 361, 422–428, https://doi.org/https://doi.org/10.1016/j.epsl.2012.11.008, 2013.

Wild, C. T., Alley, K. E., Muto, A., Truffer, M., Scambos, T. A., and Pettit, E. C.: Weakening of the pinning point buttressing Thwaites Glacier, West Antarctica, The Cryosphere, 16, 397–417, https://doi.org/10.5194/tc-16-397-2022, 2022a.

Wild, C. T., Segabinazzi Dotto, T., Alley, K. E., Collao-Barrios, G., Muto, A., Hall, R. A., Truffer, M., Scambos, T. A., Heywood, K. J., and Pettit, E. C.: A Tale of Two Ice Shelves: Contrasting Behavior During the Regional Destabilization of the Dotson-Crosson Ice Shelf System, West Antarctica, essoar[preprint], https://doi.org/10.1002/essoar.10511566.3, 2022b.

Winberry, J. P., Anandakrishnan, S., Alley, R. B., Wiens, D. A., and Pratt, M. J.: Tidal pacing, skipped slips and the slowdown of Whillans Ice Stream, Antarctica, Journal of Glaciology, 60, 795–807, https://doi.org/10.3189/2014JoG14J038, 2014.
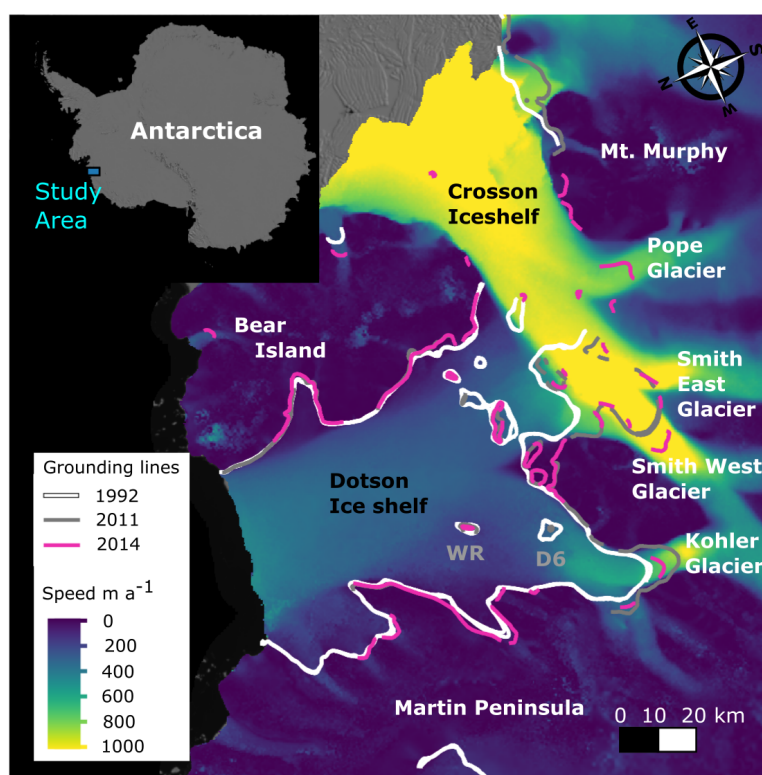
Figure 1. Ice-flow speeds for the Dotson-Crosson region from the ITS_LIVE 2018 mosaic (Gardner et al., 2018). Radar interferometry -derived grounding lines are from Rignot et al., 2014. Wunneberger Rock is shown as 'WR'.
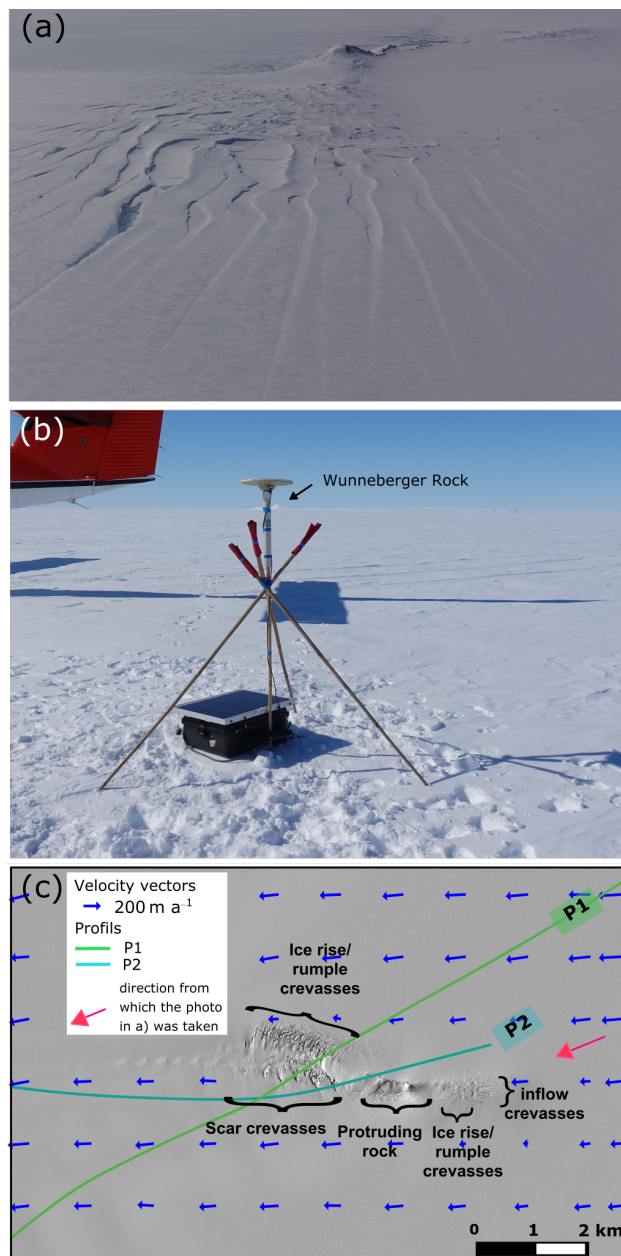
Figure 2. (a) Aerial photo of Wunneberger Rock looking northeast along the 'shark-fin' nunatak (photo courtesy: Jesse Norquay); (b) GPS installation on the Dotson Ice Shelf near Wunneberger Rock in January 2022. The nunatak can be seen in the distance next to the GPS antenna pole; (c) DigitalGlobe Worldview-2 image from November 2021 of Wunneberger Rock and surroundings showing crevassed areas, velocity vectors, and IceBridge MCoRDS L2 radar profiles location.
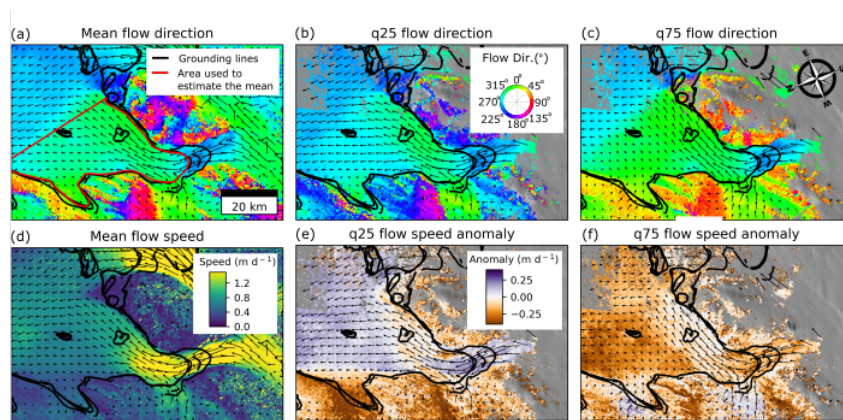
Figure 3. Dotson Ice Shelf ice direction and speed. (a), (b) and (c) show the flow direction, with colors representing different directions in polar coordinates (using the positive y direction in the EPSG 3031 projection as zero) for the mean, and 25% (q25) and 75% (q75) quartiles. d), e) and f) show the ice speed for the mean, 75%, and 25% quartile. Black lines correspond grounding lines from Rignot et al., 2014 and the red line outlines the area used to estimate the mean ice-flow direction.
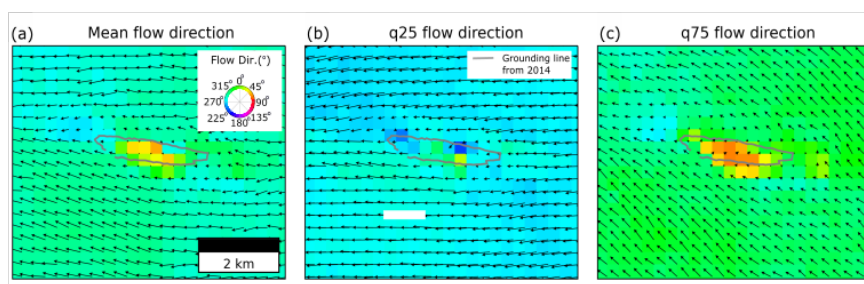
Figure 4. Detail mapping of the Dotson Ice Shelf flow direction around Wunneberger Rock, where colors represent the flow direction in polar coordinates (using the positive y direction in the EPSG 3031 projection as zero) for the mean, and 75% (q25) and 75% (q75) quartiles; (a), (b) and (c), respectively. The grounding line for 2014 is from Rignot et al. (2014).
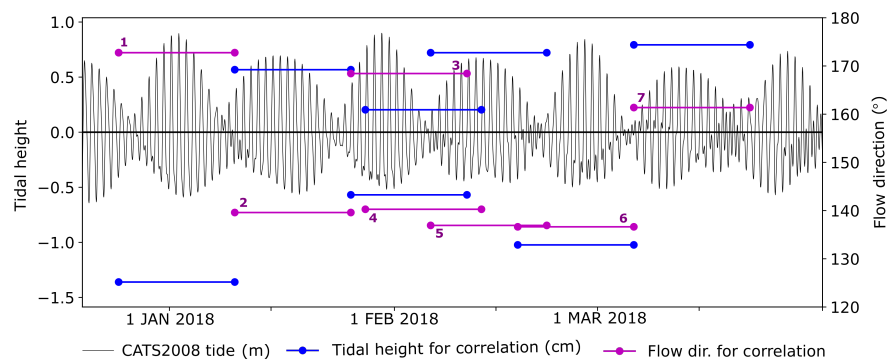
Figure 5. Tidal heights from the CATS2008 model (black line), 16-day flow direction average for correlation and 16-days average (magenta dot-line) and tide height for correlation (blue dot-line).
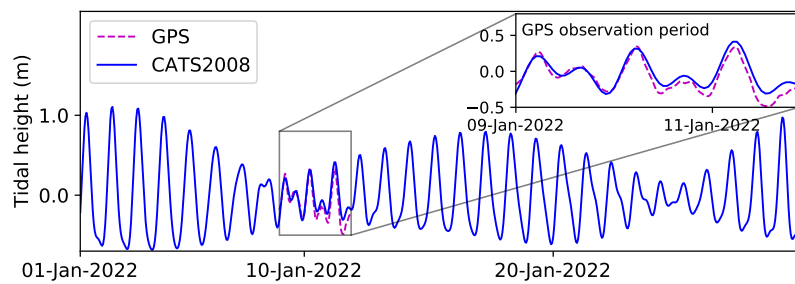
Figure 6. Tidal height from CATS2008 model and measured with the GPS during January 2022; inset, the GPS and tide model data for the 64-hour period of GPS observations.
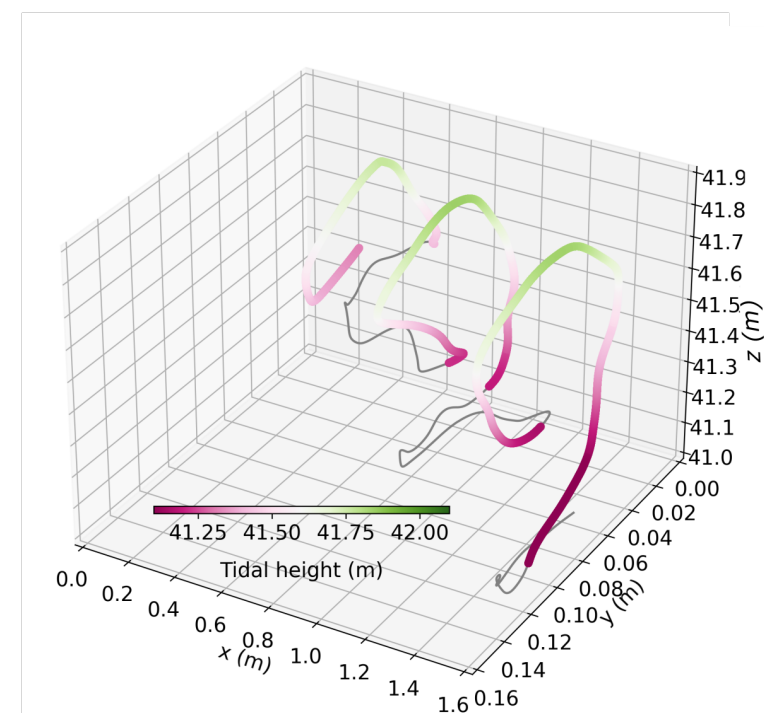
Figure 7. Three-dimensional ice motion measured using GPS, with the local flow direction coordinates aligned such that the x-axis points along the mean flow direction as determined from the GPS measurements. Colors correspond to height during the main diurnal tide component, while grey portions of the ice motion correspond to the less-pronounced semi-diurnal tide component. Note that the axes are scaled differently, particularly in the cross-flow (y) direction.
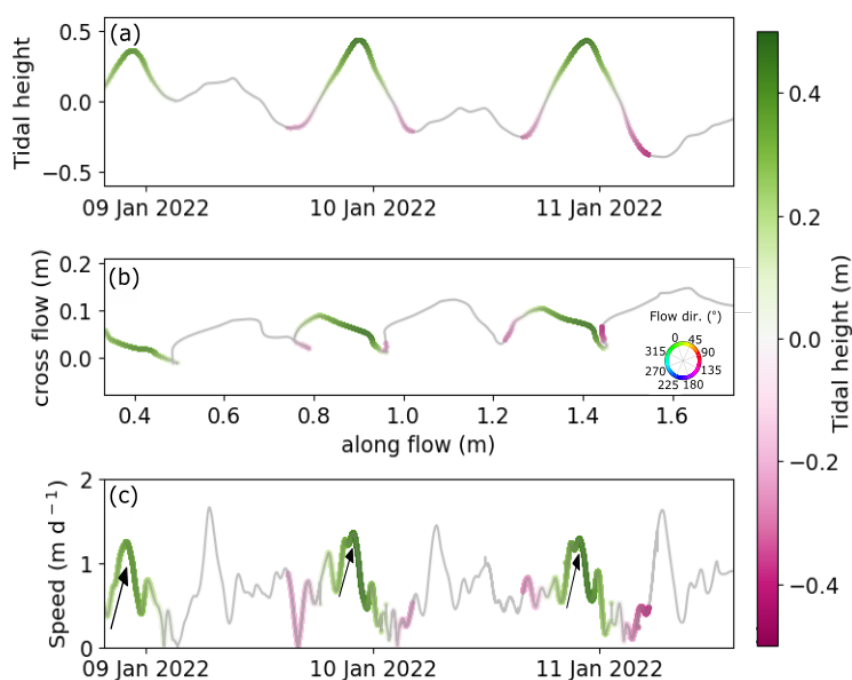
Figure 8. Tidal height and horizontal position from in-situ GPS data. Colors correspond to tidal height during the main diurnal component. Grey sections correspond to the semi-diurnal tidal component. (a) shows the measured vertical movement. (b) shows the horizontal movement on local flow direction coordinates (the colorbar corresponds to Fig.3's colorbar with EPSG 3031 projection as zero). (c) shows the measured speed and black arrows correspond to acceleration periods associated with rising tides.
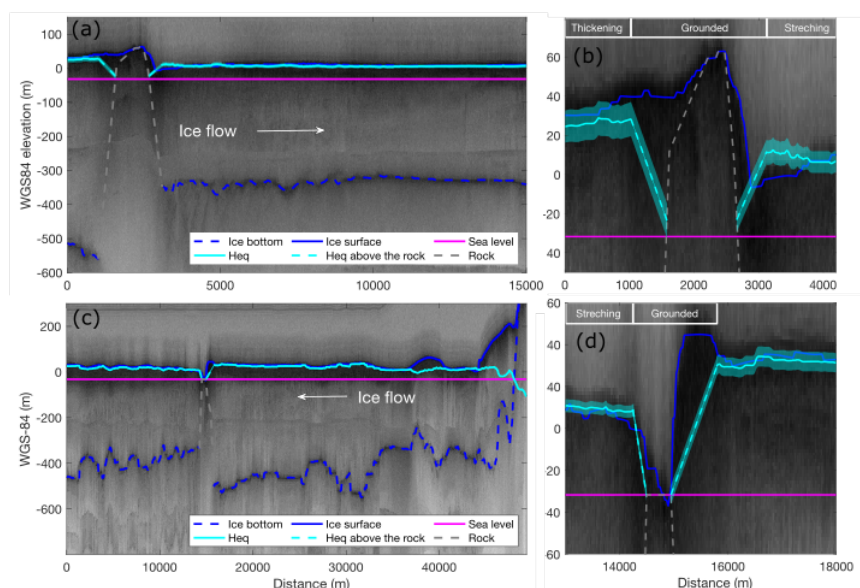
Figure 9. Radargrams from IceBridge airborne radar survey on 31 October 2018. Location is shown in Figure 2. The solid blue line corresponds to the ice surface and the dashed blue line is the interpreted ice bottom. The grey dashed lines are the approximate shape of Wunneberger Rock; magenta line is sea level from the EIGEN6c4 geoid model (Förste et al., 2014); the cyan line is the hydrostatic equivalent level assuming the ice thickness in the BedMachine data set (Morlighem, 2020); and the dotted cyan line is the hydrostatic equivalent level above the approximate shape of Wunneberger Rock.
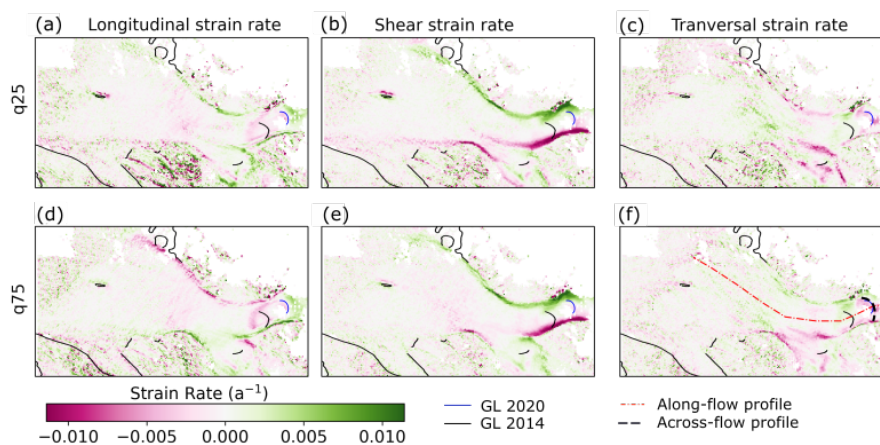
Figure 10. Longitudinal and shear strain rates for the two different tidal states and flow direction configurations. Panels a, b and c correspond to the 25% quartile representing the high tide strain patterns, with mean flow in the 290° direction. Panels d, e and f correspond to 75% quartile with mean flow in the 315° direction and low tide. The two dashed lines in panel f indicate the location of the profiles shown in Figure 11. Black line correspond to 2014 grounding line from Rignot et al., 2014 and blue line correpond to 2020 grounding line from Wild et al. (2022a).
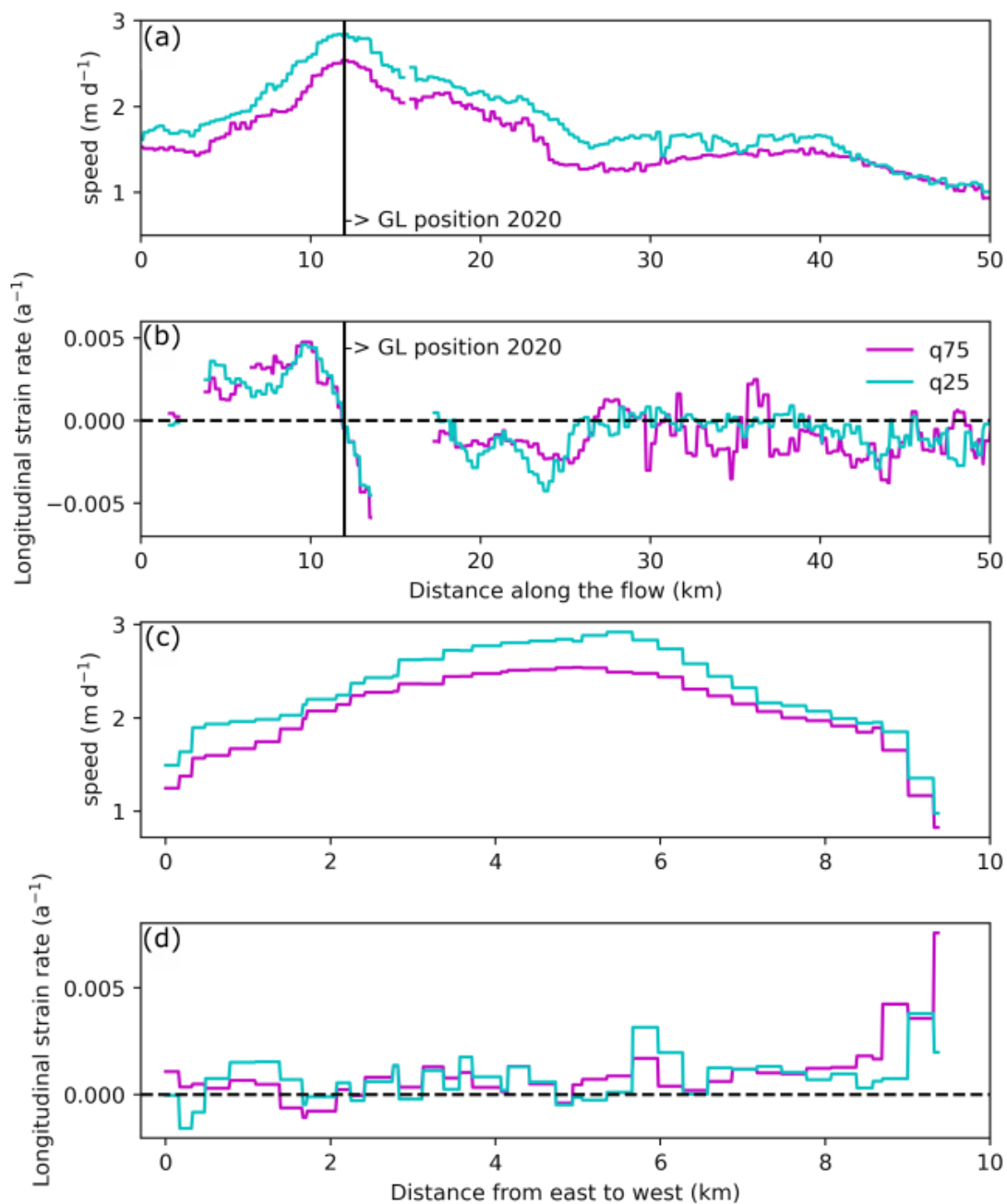
Figure 11. Speed and longitudinal strain rate in the profiles along-flow and across-flow presented in Figure 10.
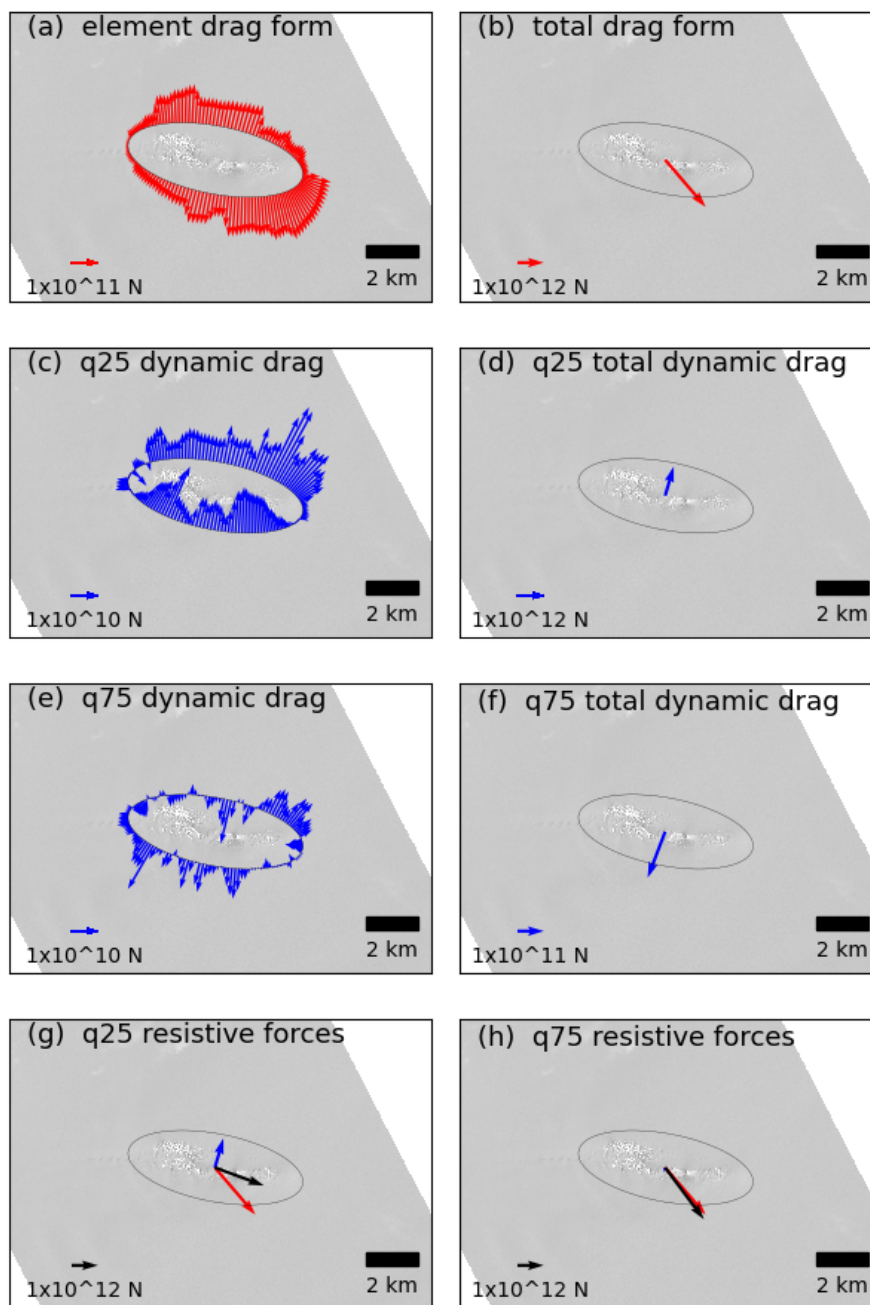
Figure 12. Wunneberger Rock force budget components as determined from the end-member ice velocity image pairs for 25% quartile (corresponding to high tide) and 75% quartile (low tide; see Figure 3): (a) form drag; (b) net form drag; (c) dynamic drag at 25% quartile; (d) net dynamic drag at 25% quartile; (e) dynamic drag at 75% quartile; (f) total dynamic drag at 75% quartile; (g) net form drag in red, net dynamical drag in blue, and total resistive force in black at 25% quartile; and (h) net form drag in red, net dynamic drag in blue, and total resistive force in black at 75% quartile (all these are closely overlapping). Grey arrows correspond to flow vectors for the ice-shelf at the respective tidal stage. Note the different scales.
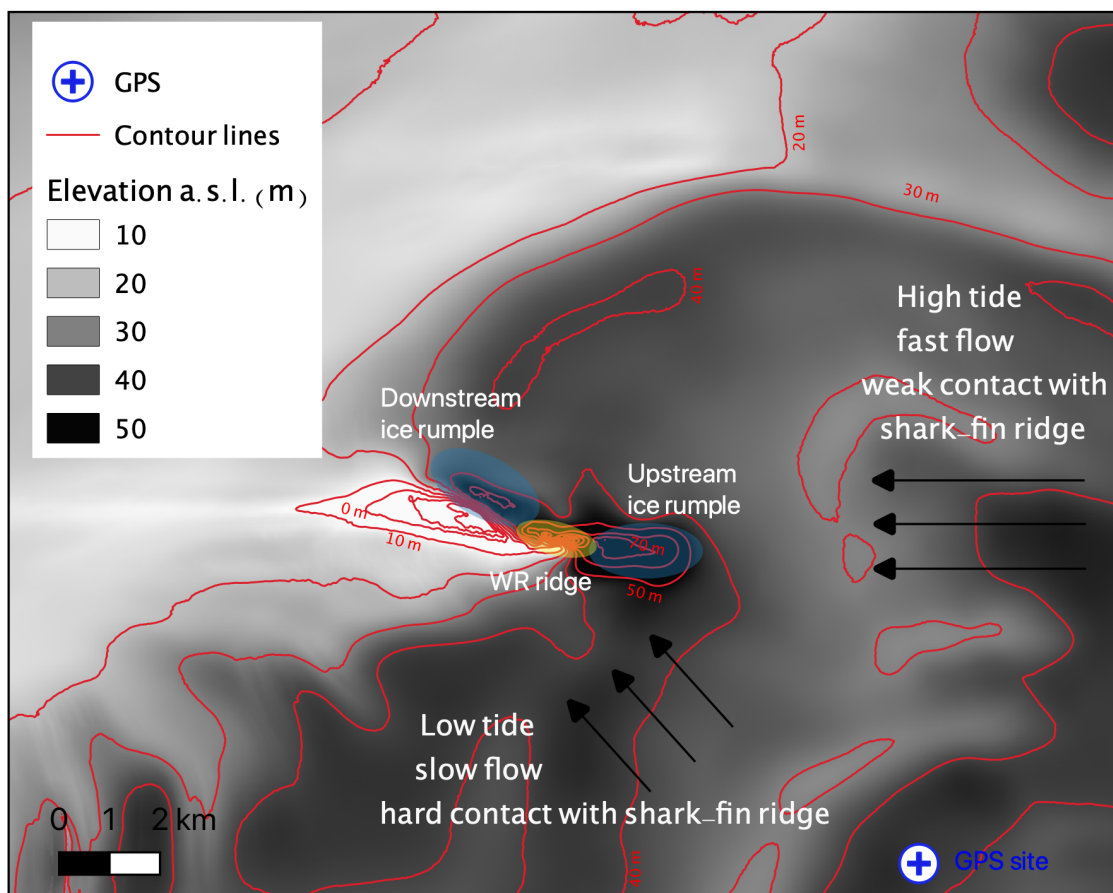
Figure 13. Scheme of the Wunneberger Rock influence on ice-flow. Ice elevation from the Reference Elevation Model of Antarctica (REMA; Howat et al. (2019)). Blue corresponds to the ice rumple zones and yellow corresponds to the shark-fin steep zone of the Wunneberger Rock pinning point.

Table 1. Table 1. Effective resistance of Wunneberger Rock

| | Form drag mag. | Dynamical drag mag. | Total drag sum mag. |
	Ff (N)	Fd (N)	Ft (N)
25% quartile	$2.30*10^{12}$	$2.00*10^{12}$	$2.00*10^{12}$
75% quartile	$2.30*10^{12}$	$0.19*10^{12}$	$2.46*10^{12}$

Figure A1. Profile along flow of tributary glacier close to Kohler Glacier. (a) Map showing profile, (b) Speed along the profile and (c) longitudinal strain rate along the profile.